Atomic resonances of hydrogen near aluminum surfaces: Adiabatic evolution of the ground state

Stefan A. Deutscher, Xiazhou Yang, and Joachim Burgdörfer
Department of Physics, University of Tennessee, Knoxville, Tennessee 37996
and Oak Ridge National Laboratory, Oak Ridge, Tennessee 37831
(Received 1 July 1996)

Complex adiabatic potential curves are an essential input to atomic surface scattering calculations employing the coupled-states method. We present calculations for the ground state of hydrogen near a jellium surface with the density of aluminum. Two complementary techniques have been implemented: the complex rotation method and the stabilization method. We employ large-scale matrix diagonalization and realistic effective single-particle potentials. The influence of the surface potential on the adiabatic evolution of the wave function and the resonance parameters as a function of the distance d from the surface have been investigated. Application to the ground state H($1s$) yields significant differences for the position and width of the resonance compared to previously available data. The applicability of semiclassical theory for resonance parameters is tested and the role of over-barrier transitions is highlighted. [S1050-2947(97)08201-2]

PACS number(s): 79.20.Rf, 34.50.Fa

I. INTRODUCTION

Resonant charge exchange between metal surfaces and ions plays an important role in many surface-diagnostic methods such as Auger electron spectroscopy, ion neutralization spectroscopy, and secondary-ion-mass spectrometry, as well as for emerging technological applications (e.g., surface catalysis, thin-film growth, and molecular-beam epitaxy). On a more fundamental level, the recent availability of electron cyclotron resonance and electron-beam ion sources delivering high intensities of low-energy multiply charged ions (MCI's) has stimulated an intense interest in the interactions of MCI's with surfaces [1]. Neutralization and relaxation of MCI's at surfaces represent an intriguing many-body problem which involves transitions of a large number of ''active'' electrons, and leads to the dissipation of large amounts of potential energy (typically $\sim$keV).

A theoretical description of dynamical ion-surface interactions requires a nonperturbative treatment, since a large number of channels (i.e., atomic states) contribute, and the perturbation is strong. Appropriate approaches are therefore the time-dependent coupled-channel calculations widely used in ion-atom collisions [2]. Application of this technique to slow ion-surface scattering involves the expansion of the time-dependent electronic wave function in terms of adiabatic states with time-dependent coefficients. The adiabatic atomic orbitals near the surface here play the analogous role of quasi-molecular orbits in slow ion-atom collisions. However, they should contain many-body effects from the outset. Most importantly, atomic states become resonances, i.e., they acquire a nonzero width because of the electron transfer to the band structure of the solid, taken to be a metal in the following. Moreover, atomic levels are shifted and strongly perturbed due to the collective response of the surface electrons.

The aim of the present contribution is the calculation and analysis of the perturbed atomic resonances corresponding to the adiabatic states at a fixed distance d from the surface. We therefore calculate the position of the resonance, i.e., the shifted energy level, its width, and its wave function, all of which are required in a coupled-channel calculation. Due to the finite velocity of the ion approaching and leaving the surface, the dynamical charge transfer process will be determined by nonadiabatic coupling between these resonances as well as with electronic states of the surface band structure, which will be considered in a subsequent paper.

At large atom-surface separations, the properties of atomic resonances can be studied by means of perturbation theory [3], and the effective atom-surface interaction potentials entering a calculation can be approximated by the asymptotic image potentials [4]. At smaller distances relevant to the charge-exchange process, perturbation theory breaks down. Nonperturbative calculations employing a Wigner-Weiskopf approximation [5,6], complex coordinate scaling (CCS) [7] and the coupled angular modes methods [8], respectively, have been reported. Irrespective of the differences in detail, previous calculations agree in the qualitative behavior: the level shift follows closely the behavior of the image potential, which suggests a promotion of the level into the continuum ($E=0$) at small distances. This shift is accompanied by a monotonic, nearly exponential, broadening of the level.

From the study of the chemisorption of hydrogen and alkali-metal atoms at metal surfaces, the static limit of atomic resonances at surfaces, i.e., in the limit of small distances ($d\rightarrow 0$) is well understood. Detailed calculations employing density-functional theory [9–14] indicate the existence of low-lying resonances embedded in the conduction band as well as of bound states below the conduction band. The connection between this $d\rightarrow -\infty$ limit and the $d\rightarrow\infty$ limit of perturbed atomic states in the image field is important, as it provides insights into the region of intermediate distances ($d\simeq 3$–5 a.u.) which are most relevant to the charge-transfer dynamics. We investigate the dependence of the resonance parameters in this intermediate region on the approximate interaction potentials, and show that an appropriate choice for the single-particle potentials is the key for establishing a smooth transition between the $d\rightarrow -\infty$ and $d\rightarrow\infty$ limits.

In this paper we employ an alternative, recently developed method for the calculation of atomic resonances which involves the stabilization technique [15,16]. One of its advantages is the direct determination of the resonant wave function, and the local density of states. The latter is required for an evaluation of coupling matrix elements for coupled-channel calculations. As a complementary method we use CCS [17–20], which provides an efficient tool for calculating complex eigenenergies (positions and widths) of atomic resonances. The comparative study permits us to gauge the accuracy and efficiency of different methods. Furthermore, since the stabilization method (SM) proceeds entirely on the real axis, larger bases can be used and the convergence as a function of basis size can be tested.

As a third method, we employ semiclassical mechanics to calculate the resonance width. Interest in the semiclassical treatment is derived from recent advances in the description of multiply charged ion-surface scattering employing the classical over-barrier model. Semiclassical methods provide a link between the classical and the full quantum descriptions, and can provide physical insight into the properties of perturbed atomic states near the surface.

In the present paper, we discuss the methods employed as well as accurate results for the adiabatic evolution of the H($1s$) resonance in front of an aluminum surface serving as a fundamental prototype system. We find well-defined over-barrier resonances, and illustrate the influence of overbarrier transitions for the position and width of the resonances. Preliminary results for $n=1$ and 2 states have been reported previously [21]. Applications to excited states $n\geqslant 2$ systems are in progress.

II. THEORY

A. Adiabatic atomic states

Within the framework of the independent-particle model for the ''active'' electron, the electronic wave function in the time-dependent Schrödinger equation

$$i\frac{d}{dt}\psi(\mathbf{r},t)=H(\mathbf{r},\mathbf{R}(t))\psi(\mathbf{r},t) \tag{1}$$

can be expanded in terms of adiabatic atomic orbitals

$$\psi(\mathbf{r},t)=\sum_j a_j(t)\,\phi_j(r,\mathbf{R}(t)) \tag{2}$$

with time-dependent expansion coefficients $a_j(t)$. The time dependence of the ϕ_j results from the parametric dependence on the classical trajectory $\mathbf{R}(t)$ of the incident ion. At finite distances from the surface $d=R_z(t)$, the orbitals are no longer purely atomic, but contain admixtures from the band structure (''hybridization''). The z axis is oriented along the surface normal. The orbitals ϕ_j incorporate many-body effects on the mean-field level. Electron-electron correlation effects are presently neglected, but could be incorporated into an expansion of the trial function in terms of Slater determinants. In the following we consider the adiabatic limit of Eq. (1),

$$H(\mathbf{r},\mathbf{p},d)\,\phi_j(\mathbf{r},d)=E_j(d)\,\phi_j(\mathbf{r},d). \tag{3}$$

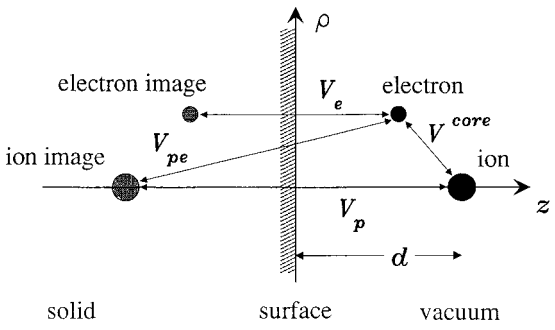

FIG. 1. Sketch of the geometry and the contributions to the potential $V^{\rm tot}$ as outlined in the text. The surface coincides with the jellium edge.

The metal will be described by a semi-infinite jellium block with a Wigner-Seitz radius of $r_s=2.07$ a.u., corresponding to the electron density of aluminum. In this model the surface coincides with the position of the jellium edge, which is defined as the plane half a lattice spacing in front of the topmost atomic layer. The origin of coordinates, $\mathbf{r}=(0,0,0)$ is placed in the surface and the atom core is located in front of the surface at $\mathbf{R}=(0,0,d)$. It is useful also to introduce a second coordinate system centered in the atom core, so that $\tilde{\mathbf{r}}=\mathbf{r}-\mathbf{R}$. Because of translation invariance in the plane of the jellium surface, the parametric dependence in Eq. (3) refers only to the distance from the surface, d. The Hamiltonian H reads

$$H=-\tfrac{1}{2}\Delta+V^{\rm tot}(\mathbf{r},d), \tag{4}$$

where Δ denotes the Laplace operator and $\mathbf{r}=(x,y,z)=(\mathbf{u},z)$ the electronic coordinates. Atomic units are used throughout ($\hbar=m_e=1$) unless otherwise stated. The total electronic potential

$$V^{\rm tot}(\mathbf{r},d)=V^{\rm core}(\tilde{\mathbf{r}})+V^{\rm surf}(\mathbf{r},d) \tag{5}$$

consists of the atomic core potential $V^{\rm core}(\tilde{\mathbf{r}})$ and of the surface potential $V^{\rm surf}(\mathbf{r},d)$. Figure 1 sketches the geometry of the system under consideration, and the various contributions to the total potential. The core potential for hydrogenic atoms with atomic number Z is a Coulomb potential $-Z/\tilde{r}$. Corresponding single-particle potentials for other atoms are available in the literature [22,23]. The surface potential for the jellium can be written as

$$V^{\rm surf}(\mathbf{r},d)=V_p(d)+V_e(\mathbf{r})+V_{\rm pe}(\mathbf{r},d), \tag{6}$$

where the first term describes the effective interaction of the ionic core (the projectile) with the surface. At large distances from the surface, this interaction converges to the classical (self)-image potential of the projectile, i.e.,

$$\lim_{d\to\infty}V_p(d)=-\frac{Z^2}{4d}. \tag{7}$$

It plays a crucial role for the image acceleration of the projectile and, hence, for the scattering dynamics [24–26], and also has to be taken into account for total-energy calculations. In the adiabatic limit, the energy positions and widths do not depend on this interaction since it is a function of only

the nuclear coordinate. Hence V_p does not enter the calculation of the resonance energies. The remaining two terms in Eq. (6) describe the electronic interaction potential with the surface, $V_e(\mathbf{r})$, which at large distances also converges to the image limit

$$\lim_{z\to\infty} V_e(\mathbf{r}) = -\frac{1}{4z}, \tag{8}$$

and the indirect interaction $V_{\rm pe}$ between the electron and the projectile through the charge-density fluctuation in the surface induced by the projectile. The asymptotic limit of the latter is given by

$$\lim_{d,z\to\infty} V_{\rm pe}(\mathbf{r},d) = \frac{Z}{\sqrt{(|z|+d)^2+u^2}}, \tag{9}$$

where $(\mathbf{u},z)$ are the cylindrical coordinates of the electron. Equation (9) describes the interaction of the electron with the image charge induced by the projectile.

The description of the interaction V_e and $V_{\rm pe}$ in terms of a local single-particle potential at intermediate interaction distances is a nontrivial problem. The choices underlying our calculations will be discussed below in more detail.

B. Calculation of resonances

For a given choice of potentials, the calculation proceeds through a large-scale basis expansion converting Eq. (3) into an N-dimensional matrix eigenvalue equation with energy eigenvalues $\{E_k\}_1^N$. Atomic (hydrogenic) basis functions are not well suited, as their positive energy subspace is not square integrable. To circumvent this problem we choose an expansion in terms of Sturmian functions [27] in the ion-centered coordinate system,

$$\Phi^{(\sigma)}_{n_r lm}(\tilde{r},\theta,\phi) = \frac{1}{\tilde{r}} S^{(\sigma)}_{n_r l}(\tilde{r}) Y^m_l(\theta,\phi). \tag{10}$$

Here n_r, l, and m denote the radial, angular, and magnetic quantum numbers, Y^m_l the spherical harmonics, and $S^{(\sigma)}_{n_r l}$ the Coulomb-Sturmian functions, given in coordinate representation by

$$S^{(\sigma)}_{n_r l}(\tilde{r}) = h_{n_r l} e^{-\sigma\tilde{r}} (2\sigma\tilde{r})^{l+1} L^{(2l+1)}_{n_r}(2\sigma\tilde{r}), \tag{11}$$

with

$$h_{n_r l} = \left(\frac{n_r!}{(n_r+2l+1)!}\right)^{1/2} \quad (n_r = n-l-1). \tag{12}$$

$L^{(\alpha)}_\mu$ in Eq. (11) are the associated Laguerre polynomials. The Coulomb-Sturmian functions contain the Sturmian parameter $\sigma = Z/n_0$, which allows for variational optimization of the basis according to the principal quantum number n of the atomic level under investigation. [For integer n_0, Eq. (10) exactly reproduces the hydrogenic wave function with the principal quantum number n_0.] The Coulomb-Sturmian basis is square integrable and (apart from the inevitable truncation) complete. Furthermore, the proximity to atomic wave functions indicates that for weakly perturbed states the expansion should rapidly converge. The price to pay for this advantage is that the basis states [Eq. (10)] form a nonorthogonal basis set which results in a generalized eigenvalue problem.

In what follows we discuss two complementary methods for determining resonance parameters from the generalized eigenvalue matrix equation

$$\underline{\underline{H}}\,\underline{\phi}^{(\sigma)}_j = E_j \underline{\underline{N}}\,\underline{\sigma}^{(\sigma)}_j, \tag{13}$$

where $\underline{\underline{H}}$ and $\underline{\underline{N}}$ are the Hamiltonian and the nonorthogonality (overlap) matrix for the basis of Eq. (10). The matrix elements can be expressed analytically with the exception of $\langle i|V^{\rm surf}|j\rangle$, which must be computed numerically.

Equation (13), as it stands, gives only discrete real eigenvalues $\{E_j\}$ of bound states. One standard method for the calculation of resonances is complex coordinate scaling, which corresponds to a canonical transformation in the complex plane

$$\tilde{\mathbf{r}} \to \tilde{\mathbf{r}} e^{i\Theta}, \tag{14a}$$

$$\mathbf{p} \to \mathbf{p} e^{-i\Theta}. \tag{14b}$$

This converts resonant (continuum) wave functions into square-integrable functions by effectively projecting out the P space (continuum space) portion of the wave function. Consequently, the Hamiltonian becomes dependent on the complex rotation angle Θ,

$$H(\tilde{\mathbf{r}},\mathbf{p}) \to H(\tilde{\mathbf{r}},\mathbf{p},\Theta) = -\tfrac{1}{2} e^{-2i\Theta}\Delta + V^{\rm tot}(\tilde{\mathbf{r}} e^{i\Theta}). \tag{15}$$

$H(\tilde{\mathbf{r}},\mathbf{p},\Theta)$ is no longer Hermitian, and Eq. (13) yields complex eigenvalues. Thresholds (in our case corresponding to the continua at the bottom of the conduction band, $V_0<0$, and at the ionization threshold $E=0$) are rotated into the complex plane by an angle of 2Θ, thus exposing the resonances, while bound states remain on the real axis. Converged resonances are characterized by the stability of the complex eigenvalue $E=E_r-i\Gamma/2$ with respect to the rotation angle Θ, the Sturmian parameter σ, and the basis size N. The analytic continuation of the potential $V^{\rm tot}(\tilde{\mathbf{r}}e^{i\Theta})$ into the complex plane is explicitly known only in simple cases. While the mathematical foundation of the method, the Aguilar-Baslev-Combes theorem [17], strictly holds only for dilatation-analytic potentials, ample evidence exists that the method is applicable to a much wider range of potentials. For realistic surface potentials we adopt the ''passive'' rather than the ''active'' complex rotation, rotating the wave function $\Phi_{n_r lm}(\tilde{\mathbf{r}}e^{-i\Theta})$ instead of the Hamiltonian. However, one conceptual difficulty of the passive complex rotation is that the physical interpretation of the resonant wave function is less obvious.

A recently developed attractive alternative method [15,16] uses the fact that stabilization diagrams, well known as a tool for the determination of the positions of resonances, can also reveal information on their widths. One advantage is that the calculation proceeds on the real axis, and the determination of the resonant wave function is straightforward. This method comes with the added benefit that the calculation on the real axis permits the use of comparatively larger basis sizes.

The spectral density of resonances (the Feshbach Q space complement [28]) is given by

$$D^Q(E) = -\frac{1}{\pi}\,\mathrm{Im}\left(\sum_k \frac{1}{(E-E_k)+i\Gamma_k/2}\right), \qquad (16)$$

with $E_k - i\Gamma_k/2$ the complex poles of the Green's function. $D^Q(E)$ can be calculated by repeated diagonalization of Eq. (13) on the real axis (i.e., $\Theta=0$) for a range of σ values $\sigma\in[\sigma_{\min},\sigma_{\max}]$, yielding σ-dependent sets of eigenvalues $\{E_k(\sigma)\}_1^N$. The spectral density follows from

$$D^Q(E) = -\frac{1}{\sigma_{\max}-\sigma_{\min}}\int_{\sigma_{\min}}^{\sigma_{\max}} d\sigma\; D_\sigma(E), \qquad (17)$$

where

$$D_\sigma(E) = \sum_j \delta(E_j(\sigma)-E). \qquad (18)$$

Equation (17) is readily evaluated in terms of these $E_j(\sigma)$ as

$$D^Q(E) = -\frac{1}{\sigma_{\max}-\sigma_{\min}}\sum_j \left|\frac{dE_j(\sigma)}{d\sigma}\right|^{-1}_{E_j(\sigma)=E}. \qquad (19)$$

$D^Q(E)$ can also be obtained by binning all energies $E_j(\sigma)$ for $\sigma_{\min}\leqslant\sigma\leqslant\sigma_{\max}$ into a histogram and then fitting a smooth function. Figure 2(a) displays a typical stabilization diagram for hydrogen in front of an aluminum surface. The resulting histogram from which the spectral density $D^Q(E)$ can be determined is shown in Fig. 2(b). Equation (19) can be visualized as a projection of the line density of the stabilization diagram onto the energy axis. From the fit of the ''raw'' spectrum of Eq. (19) to a sum over Lorentzian lines (including a linear background), both positions E_k and widths Γ_k can be extracted with high accuracy. Moreover, unlike in the CCS, the resonant wave functions can be directly determined. The local spectral density of the corresponding resonance wave function $|\phi_k^Q(\tilde{\mathbf{r}};E_k)|^2$ at the energy E_k, is analogous to Eq. (19) given by

$$|\phi_k^Q(\tilde{\mathbf{r}};E_k)|^2 = \frac{1}{\sigma_{\max}-\sigma_{\min}}\sum_j |\phi_j(\tilde{\mathbf{r}},\sigma)|^2\left|\frac{dE_j(\sigma)}{d\sigma}\right|^{-1}_{E_j(\sigma)=E_k}. \qquad (20)$$

The evaluation of the sum Eq. (20) over all j wave functions ϕ_j each containing up to $\simeq 10^3$ terms of the Sturmian expansion [see Eq. (10)] is extremely time consuming. In practice, only a few states ϕ_j in the immediate vicinity of E_k, i.e., with the largest slope $|dE_j(\sigma)/d\sigma|^{-1}$, can be taken into account. Knowledge of the local spectral density and of the resonant wave function is valuable for the physical interpretation of resonances.

III. SURFACE POTENTIALS

An important input for the calculation are the potentials V_e and V_{pe}. Differences among different calculations [7,8,21] are in part due to different choices for these potentials. The present approximations are motivated by the aim to employ functional forms that smoothly interpolate between the image potential limits at large distances ($d\to\infty$) and the effective potential of a hydrogen atom embedded in jellium, as determined by density-functional theory [11,13,29]. In this section, we use again the coordinate system centered in the surface plane, i.e., $z=0$ coincides with the jellium edge.

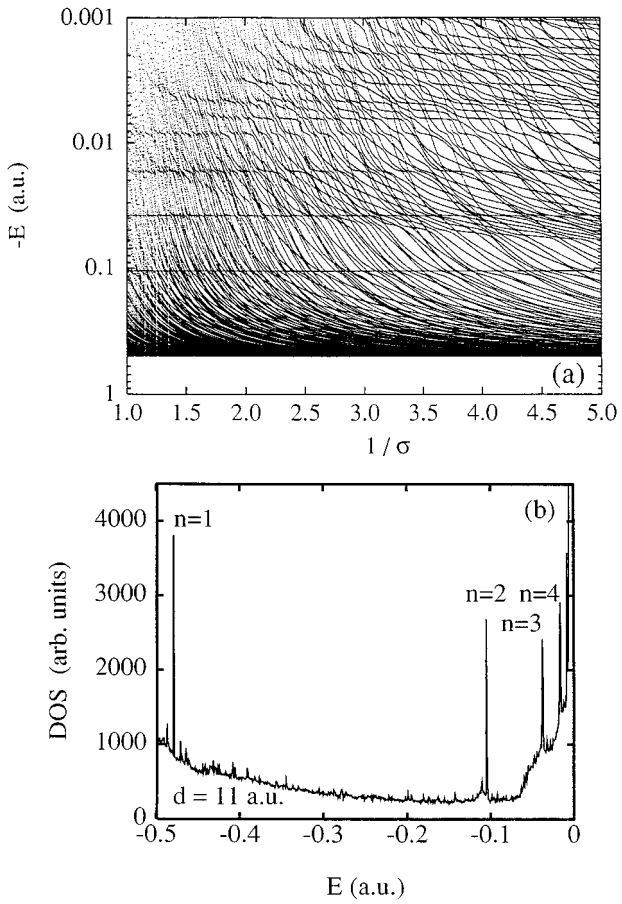

FIG. 2. (a) Typical stabilization diagram for a hydrogen ($Z=1$) atom at $d=11$ a.u. in front of an aluminum surface: energy E as a function of the inverse Sturmian parameter, $1/\sigma$. Stabilized horizontal ''lines'' correspond to resonances, e.g., near $E=-0.1$ a.u. for $n=2$. Resonances up to $n=8$ can be clearly distinguished. (b) Density of states (DOS) extracted from the data shown in (a).

A. Electronic surface potential

For the electron-jellium surface interaction V_e we use the model potential proposed by Jennings, Jones, and Weinert [30]:

$$V_e(z) = -\frac{1}{2}\begin{cases}\dfrac{1-\exp[-\lambda(z-z_0^e)]}{2(z-z_0^e)} & \text{if } z>z_0^e\\[2ex] \dfrac{2V_0}{A\,\exp[B(z-z_0^e)]+1} & \text{otherwise,}\end{cases} \qquad (21)$$

where $A=-4V_0/\lambda-1$ and $B=-2V_0/A$ are constants determined by matching the potential and its derivative at $z=z_0^e$.

In the limit $z\to\infty$, Eq. (21) converges to the proper self-image limit, correct to order $O(z^{-2})$,

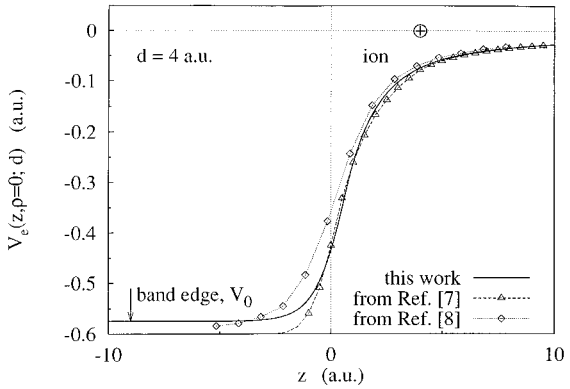

FIG. 3. Electronic self-image potential near an Al surface ($d=4$ a.u.), — this work, --- Nordlander and Tully [7], ⋯ Borisov, Teillet-Billy, and Gauyacq [8].

$$\lim_{z\to\infty} V_e(z) = -\frac{1}{4(z-z_0^e)}. \tag{22}$$

The coordinate z_0^e defines the position of the image plane. Its numerical value of a jellium with a Wigner-Seitz radius of $r_s=2.07$ is $z_0^e=0.7$. The constants V_0 (energy at the bottom of the conduction band) and λ are chosen such as to reproduce for small z the self-consistent local-density approximation (LDA) of Kohn and Lang [11] near and inside the surface (apart from the Friedel oscillations). It should be noted that, within the fit to Eq. (21), z_0^e is influenced by the behavior of the potential at intermediate distances. Somewhat larger values have been found in calculations extracting z_0^e from the asymptotic behavior of the z^{-2} term [31–34]. Figure 3 displays V_e together with the corresponding potentials chosen in previous calculations [7,8]. Overall, the potential functions are very similar. The deviations stem mainly from the slightly larger value for $z_0^e \simeq 0.85$ and from a different r_s value, $r_s=2.0$, which lowers V_0 from $V_0=-0.574$ to $V_0=-0.604$. None of these differences, however, have a profound influence on the resonance parameters.

B. Ionic surface potential

Much more pronounced differences originate from the projectile-induced surface potential $V_{\rm pe}(\mathbf{r},d)$. It consists of an electrostatic (el) term and an exchange-correlation (xc) term [11],

$$V_{\rm pe}(\mathbf{r},d) = V_{\rm el} + V_{\rm xc}. \tag{23}$$

Both terms are determined by the density fluctuation $\varrho_{\rm ind}(\mathbf{r},d)$ at the jellium surface induced by a proton located at a distance d from the surface. The electrostatic term reads

$$V_{\rm el} = \int d^3r' \, \frac{\varrho_{\rm ind}(\mathbf{r}',d)}{|\mathbf{r}-\mathbf{r}'|}. \tag{24}$$

The exchange and correlation term $V_{\rm xc}$, which contributes only at small distances from the surface, is given by the change of the chemical potential $\mu_{\rm xc}$ due to the presence of the charge density $\varrho_{\rm ind}$ induced in the surface by the external charge Z,

$$V_{\rm xc} = \mu_{\rm xc}[\varrho] - \mu_{\rm xc}[\varrho_0], \tag{25}$$

where $\varrho=\varrho_0+\varrho_{\rm ind}$ and ϱ_0 is the electron density of the unperturbed electron gas taken from calculations in the LDA [11]. Keeping only the term linear in $\varrho_{\rm ind}$ of the Taylor series expansion for $\mu_{\rm xc}[\varrho]$, we obtain

$$V_{\rm xc} = \left(\frac{d}{d\varrho}\,\mu_{\rm xc}\right)_{\varrho_0} \varrho_{\rm ind}(\mathbf{r},d). \tag{26}$$

The chemical potential $\mu_{\rm xc}$ can be expressed as

$$\mu_{\rm xc} = \frac{d}{d\varrho}\,(\varrho\,\varepsilon_{\rm xc}[\varrho]). \tag{27}$$

For the exchange-correlation energy $\varepsilon_{\rm xc}$ we used the expression from [9,10,35] in terms of $r_s(\varrho)=(3/(4\pi\varrho))^{1/3}$,

$$\varepsilon_{\rm xc}(r_s[\varrho]) = -\frac{0.458\,16}{r_s} - \frac{0.442}{r_s+7.8}. \tag{28a}$$

For comparison we also tested

$$\epsilon_{\rm xc}(r_s[\varrho]) = -\frac{0.458\,16}{r_s} + 0.0311\,\ln r_s - 0.048, \tag{28b}$$

as given in [36]. The resulting expressions for $\mu_{\rm xc}$ are

$$\mu_{\rm xc}(r_s[\varrho]) = -\frac{4}{3}\frac{0.458\,16}{r_s} - \frac{0.442}{r_s+7.8}\left(1+\frac{r_s}{3(r_s+7.8)}\right) \tag{29a}$$

and

$$\mu_{\rm xc}(r_s[\varrho]) = -\frac{4}{3}\frac{0.458\,16}{r_s} + 0.0311\,\ln r_s - 0.058\,35, \tag{29b}$$

respectively, which differ from each other for the bulk density of Al by less than 4%.

Our approximation of $\varrho_{\rm ind}$ exploits the fact that the density profile along the surface normal, $g(z,d)$ (integrated over the coordinate $\mathbf{u}$ in the surface plane) is for $|Z|=1$ accurately known from density-functional (DF) calculations [33,34]. The induced charge density entering Eq. (23) which smoothly interpolates between the bulk limit ($d\to-\infty$), and the asymptotic image limit ($d\to\infty$) is written as a superposition

$$\varrho_{\rm ind}(\mathbf{r},d) = c_1\varrho^B(\mathbf{r},d) + c_2\varrho^I(\mathbf{r},d). \tag{30}$$

Here ϱ^B converges to the induced density in the bulk ($d\to-\infty$), while ϱ^I is the induced density in the image limit ($d\to\infty$). Accordingly, we choose the coefficients $c_1=e^{-d/\kappa}$ and $c_2=1-c_1$, where $\kappa=1.5a_{\rm TF}$ and $a_{\rm TF}=(\pi/12)^{2/3}r_s=0.8471$ a.u. denotes the Thomas-Fermi screening length [37]. For ϱ^B we use the functional form

$$\varrho^B(\mathbf{u},z;d) = c\,\exp(-\sqrt{a^2u^2+b^2(z-z_B)^2}) \tag{31}$$

where a, b, and z_B are distance-dependent parameters, while $c=a^2b/(8\pi)$ is a normalization factor. a and b are related to

the inverse screening length of aluminium in lateral and perpendicular directions. In the bulk limit the screening is isotropic, i.e., $a=b$. We obtain a, b, and z_B at $d=0$ and $d=1.89$ from fits to the averaged charge density $g(z,d)$ determined by DF theory [31,33,34]. Extrapolation of $a(d)$, $b(d)$, and $z_B(d)$ to larger distances d is performed by using the scaling relation of the Thomas-Fermi screening length with the (unperturbed) distance dependent local electron density, $a_{\mathrm{TF}} \propto n^{-1/6}$.

In order to reproduce the correct asymptotic image limit, we write the density fluctuation for proton positions outside the surface ($d>0$) in separable form,

$$\varrho^I(\mathbf{r},d)=f(\mathbf{u},d)g(z,d), \tag{32}$$

where f describes the lateral charge-density fluctuation in the surface plane, which we calculate within the framework of the linear dynamical response formulation of Abajo and Echenique [38]. Writing $\mathbf{r}=(\mathbf{u},z)$ for the position of the electron and $\mathbf{k}=(\mathbf{Q},k_z)$ for the wave vector, where $\mathbf{u}$ and $\mathbf{Q}$ denote the components of $\mathbf{r}$ and $\mathbf{k}$ parallel to the surface, the dynamical screening potential of an ion of charge Z located at a distance d outside the solid is given in the zero-velocity (adiabatic) limit by

$$V^I_{\mathrm{pe}}(\mathbf{r},d)=\frac{Z}{2\pi}\int d^2Q\,\frac{e^{i\mathbf{Q}\cdot\mathbf{u}}}{Q}\begin{cases}\dfrac{\epsilon_S(Q,0)-1}{\epsilon_S(Q,0)+1}\,e^{-Q(z+d)}+e^{-Q|z-d|} & \text{if } z>0 \quad \text{(vacuum)}\\ \dfrac{2\epsilon_S(Q,z,0)}{\epsilon_S(Q,0)+1}\,e^{-Qd} & \text{if } z<0 \text{(solid)},\end{cases} \tag{33}$$

where $\epsilon_S(Q,\omega)=\epsilon_S(Q,z=0,\omega)$ is the surface dielectric response function [39,40] related to the bulk dielectric function ϵ_B by

$$\epsilon_S(Q,z,\omega)=\frac{Q}{\pi}\int_{-\infty}^{\infty}\frac{dk_z e^{ik_z z}}{(k_z^2+Q^2)\epsilon_B(\mathbf{k},\omega)}. \tag{34}$$

For our calculations we have used the surface-plasmon-pole approximation with dispersion [40]

$$\epsilon_S(Q,\omega)=1+\frac{\omega_p^2}{\alpha Q+\beta Q^2+Q^4/4-(\omega+i\gamma)\omega}, \tag{35}$$

where $\omega_s=\omega_p/\sqrt{2}$ is the surface-plasmon frequency, and γ describes phenomenologically the width of the surface-plasmon resonance [41,42]. In the static case ($\omega=0$) considered here, ϵ_S is independent of γ. The surface-plasmon dispersion for small Q is governed by the parameters α and β. The standard values are $\alpha=\sqrt{3/10}v_F\omega_p$ ($\alpha=0.269$ a.u. for Al), with β chosen such that the resulting dispersion curve is consistent with the bulk dispersion curve at its point of intersection with the single-particle continuum [40]. The value of α determines the linear slope of the dispersion curve. A more realistic value extracted from experimental data for the surface plasmon dispersion of Al [43] is $0.1\leqslant\alpha\lesssim 0.18$.

From Poisson's equation now follows the induced charge density corresponding to Eq. (33). Neglecting the z dependence in ϵ_S by setting $z=0$ in Eq. (34), we obtain

$$n(\mathbf{r},d)=\delta(z)\left[\frac{Z}{4\pi^2}\int d^2Q e^{i\mathbf{Q}\cdot\mathbf{u}}\,\frac{1-\epsilon_S(Q,0)}{1+\epsilon_S(Q,0)}\,e^{-Qd}\right]. \tag{36}$$

The fact that the density along the surface is localized in a δ-shaped charge-density sheet centered at the jellium edge is a consequence of the z independence of $\epsilon_S(Q,\omega)$. This additional approximation has the advantage that it yields an explicit expression for the lateral distribution $f(\mathbf{u},d)$ [Eq. (3)]. Without directly affecting our calculation since the sheet of zero thickness will be replaced in our treatment by the density profile $g(z,d)$ [Eq. (32)]. It should be noted that without the simplifying assumption $z=0$ in $\epsilon_S(Q,z,\omega)$, the specular reflection method (SRM) yields, instead of the δ-shaped charge sheet centered on the surface, an exponentially decreasing polarization charge density as a function of distance z into the metal [38], while it cannot account for the spilling out of charge density into the vacuum. The resulting lateral charge density (averaged over z) differs only marginally from the one obtained from

$$f(\mathbf{u},d)=\frac{Z}{4\pi^2}\int d^2Q e^{i\mathbf{Q}\cdot\mathbf{u}}\,\frac{1-\epsilon_S(Q,0)}{1+\epsilon_S(Q,0)}\,e^{-Q(\mathbf{d}-z_q(d))}. \tag{37}$$

In Eq. (37) we have explicitly taken into account that the induced charge density ''spills out'' of the jellium edge by measuring the distance from the ion relative to the centroid of the charge distribution along the surface normal [see Eq. (40) below] rather than to the jellium edge.

The realistic density fluctuation profile along the surface normal z enters Eq. (32) through $g(z,d)$, which we parametrize in terms of a skewed Lorentzian

$$g(z,d)=a_1\,\frac{1+a_2(z-a_4)}{(1+a_3(z-a_4)^2)^3}. \tag{38}$$

The d-dependent parameters a_i in Eq. (38) are subject to the constraint of normalization,

$$\int dz\; g(z,d)=1, \tag{39}$$

and to the constraint of reproducing the correct position z_q of the centroid of the charge density fluctuation, closely related to but not identical with the image plane position,

$$\int dz\; g(z,d)z=z_q(d). \tag{40}$$

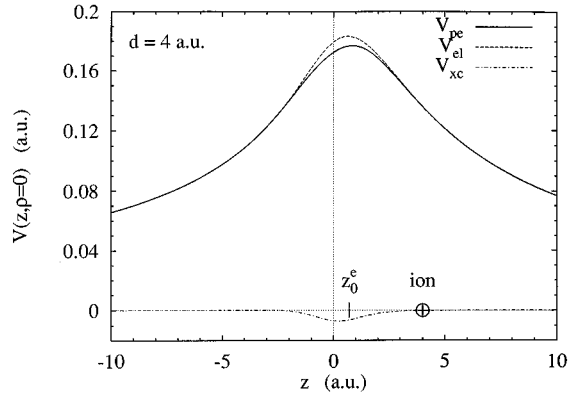

FIG. 4. Electron-ion image potential for H^+ near an Al surface ($d=4$ a.u.) (—, V_{pe}) and its two contributions (---, V_{el}; -·-·- V_{xc}).

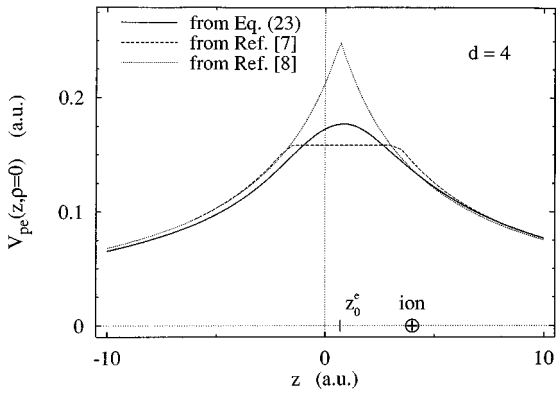

FIG. 5. Electron-ion image potential V_{pe} for H^+ near an Al surface ($d=4$ a.u.): —, present work; ---, from [7], ⋯ , image potential as used in [8].

For test purposes we also utilized a parametrization in terms of a Gaussian function instead of Eq. (38), which leads to only minor differences. It should be noted that unlike for small distances, where we use ϱ^B [Eq. (31)], the separable approximation [Eq. (32)] to the density fluctuation should be valid at large distances. Inserting Eq. (30) into Eq. (23) leads to the total potential V_{pe} entering the calculation.

The present approximation incorporates several important features of a realistic electron surface response: V_{pe} remains finite as $r\to 0$ and $d\to 0$. It therefore avoids the well-known difficulties with the singular behavior of the classical image potential. The residual effect of this singularity makes itself felt even at intermediate distances from the surface, where charge transfer in ion-surface scattering takes place (the critical distance for overbarrier transitions or ''freezing'' distance [26,44]). In the limit of small distances it reproduces the charge-density fluctuation of the LDA. At the same time, it reproduces the correct asymptotic limit at large distances to order d^{-2}, i.e., it contains the image interaction with the approximate position of the image plane outside the jellium edge. Expansion of Eq. (23) to order d^{-2} leads to a position of the image plane

$$z_0^i = z_q(d\to\infty) - \frac{\alpha}{2\omega_s^2}. \tag{41}$$

For small α ($\simeq 0.1$) the values of $z_q(d\to\infty)$ and z_0^i approximately agree, and by an appropriate choice of $z_q(d\to\infty)$ the ionic and electronic image planes can be made to coincide at large distances, $z_0^i, z_0^e \to z_0$. Note, however, that due to the different nature of these two contributions to the induced charge density, the two image planes need not necessarily coincide at small distances. Furthermore, the u dependence of the lateral density fluctuations representing virtual surface-plasmon excitations is consistent with the experimental data for the on-shell surface-plasmon description.

We note that the second term in Eq. (41), $-\alpha/2\omega_s^2$, corresponds to the effective image plane position of just the SRM model for the electrostatic potential [Eq. (33)]. Using only this term, the correct image plane position could also be reproduced by Eq. (33) provided one chooses a large negative α ($\alpha=-0.6$ for Al), as was pointed out by Annett and Echenique [45]. Such a choice is, however, inconsistent with the experimental data on surface-plasmon dispersion for Al [41,43], and is unsatisfactory since positive values of z_0^i are primarily due to the spilling out of the screening charge [Eqs. (30) and (38)] rather than due to an anomalous plasmon dispersion in the surface plane.

Figure 4 displays the resulting potential V_{pe} and its electrostatic (el) and exchange (ex) contribution at a distance $d=4$. The electrostatic potential strongly dominates the exchange contribution. The latter becomes only significant for $d\lesssim 2$, where a more accurate determination would require a self-consistent treatment. A comparison (Fig. 5) between the potential V_{pe} used in our calculations and choices in previous calculations indicates that the potential used in Ref. [8] closely mimics the singular behavior of the classical hydrogen potential near the image plane. Our potential agrees considerably better with Ref. [7], showing a broad maximum near $z=0$. The shape is, however, different primarily due to the fact that the density fluctuation in Ref. [7] was determined by the classical charge density rather than by linear-response theory.

The d dependence of the resulting total potential V^{tot} including all surface potential terms as well as the bare

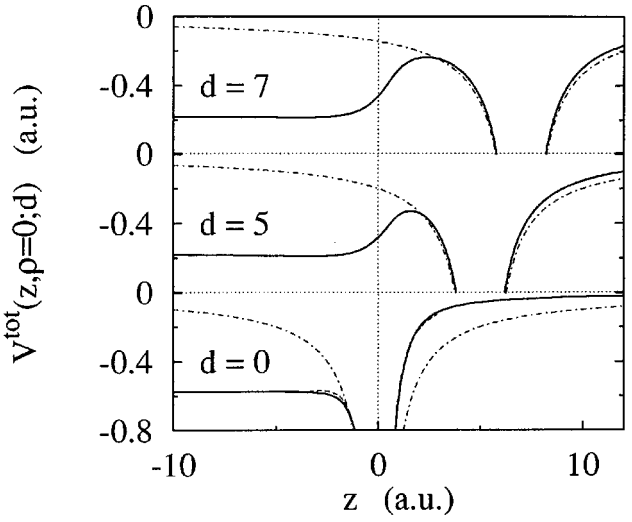

FIG. 6. Total surface potential $V^{tot}(z,u;d)$ for H near an Al surface at cut along $u=0$ for $d=7$, 5, and 0 a.u. (—). For comparison, also shown are the bare core potential V^{core} (-·-·-) and for $d=0$ the total potential within the LDA V^{tot} from [13] (---), which nearly coincides with our data.

projectile-electron term is illustrated in Fig. 6 for cuts ($\mathbf{u}=\mathbf{0}$) through the potential surface, and for distances $d=7$, 4, and 0. The last frame is of particular interest as self-consistent calculations for V^{tot} in the LDA are available for small d [13]. (Note that the LDA fails at larger d because of the lack of induced long-range potential contributions). The agreement between our (though not self-consistent) potential with the LDA result even at very small $d\simeq 0$ is unexpectedly good. This provides a clear indication that the potential function should be sufficiently accurate at intermediate distances $d\gtrsim 3$, which are most significant for dynamical charge transfer.

With decreasing distance from the surface, the barrier separating the atomic well from the jellium is rapidly reduced in height. We therefore anticipate that hydrogenic resonances become over-barrier resonances near the surface. Contrary to conventional wisdom, tunneling plays a role only at distances large compared to typical freezing distances; this statement applies even more so to higher excited states [46].

IV. QUANTUM-MECHANICAL RESULTS

Our resonance calculations have been performed for 56 values of the rotation angle ranging from $\Theta=0.05...0.60$ rad, and for about 1500 values of the stabilization parameter σ^{-1} in the interval $1.0\leqslant\sigma^{-1}\leqslant 6.0$ in the case of the stabilization method. Detailed convergence tests were made with respect to the basis size $N\in[8,N_{\max}]$ and the choice of the Sturmian parameter $\sigma^{-1}\in[0.2, 10.0]$. We used up to $N_{\max}=1891$ basis states for the complex rotation, and up to $N_{\max}=4096$ for the stabilization method. At small distances the resonance parameters are most sensitive to the basis size and the Sturmian parameter when the resonance has become an over-barrier resonance. An example for the convergence behavior is given in Fig. 7 for $d=2$. While at this small distance the potential cannot be considered reliable, this example illustrates the characteristic sensitivity of over-barrier resonances. The ground state was found to be more sensitive to the proper choice of σ than were excited states which, in turn, were more sensitive to the basis size than the ground state. The level position for the $1s$ state converged faster than the width, which, for $d=2$ a.u., already required 496 basis states for sufficient accuracy (Fig. 7). In order to achieve convergence for the ground state for all $d>2$ to three significant digits, a basis size of about $N_{\max}=500$ with an optimized Sturmian parameter was required. We note that this number is significantly larger than in previous calculations [7]. Higher excited states require even larger basis sets to allow a proper representation of the resonant portion of the electron wave function.

We find the CCS and SM to be of comparable accuracy for the present problem. Typically, resonance parameters are converged to a relative error of $\simeq 10^{-3}$. It should be stressed that the uncertainties due to the choice of the potential functions are much larger. We find the CCS more efficient for the simultaneous calculation of both the position ($\mathrm{Re}\,E_j$) and the half-width ($-\mathrm{Im}\,E_j$). On the other hand, the SM is faster when only the level position is required. It also permits more comprehensive convergence tests with respect to larger basis sizes.

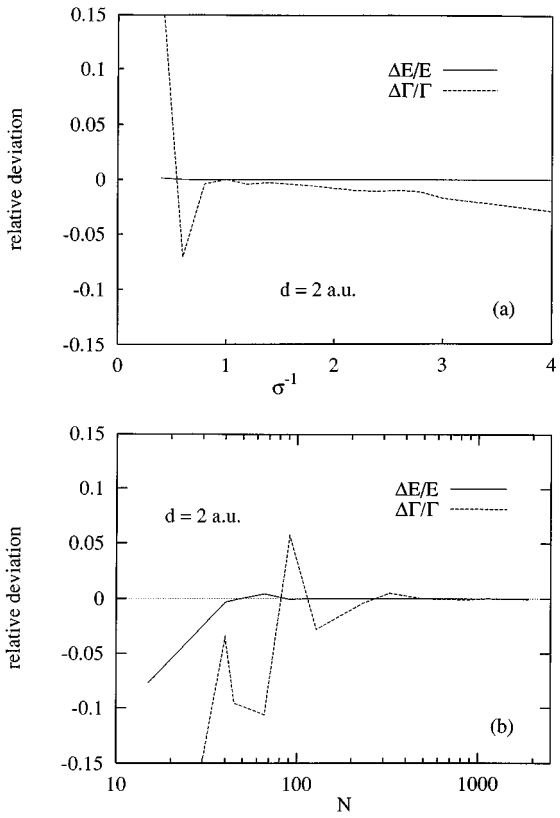

FIG. 7. Convergence of the ground-state resonance energy (solid line) and width (dashed line) at $d=2$ a.u. as a function of the inverse Sturmian parameter $1/\sigma$ and the basis size N: (a) Relative deviation with respect to the values for $\sigma=1$ vs inverse Sturmian parameter $1/\sigma$ for $N=231$. (b) Relative deviation with respect to the values for $N_{\max}$ vs basis size N for $\sigma=1$.

A. Level position

The real part E_r of the complex eigenenergy of the resonance, i.e., the position of the $1s$ level (Fig. 8), approaches for large d the simple ''image limit,'' $E_{1s}(d)=E_{1s}(\infty)+1/(4(d-z_0))$, predicted by first-order perturbation theory. For small and intermediate distances our results deviate significantly—even on a qualitative level—from pertur-

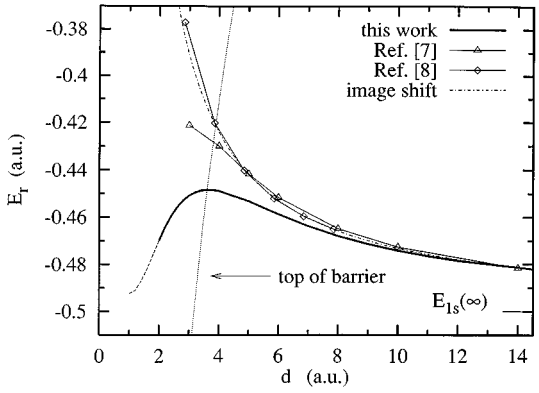

FIG. 8. Position of the H($1s$) resonance [$E_r=\mathrm{Re}(E)$] near an Al as function of d: —, present results; △, Ref. [7]; ◇, Ref. [8]; -·-·-, image shift formula $E_{1s}(\infty)+[1/4(d-z_0)]$. Also shown is the energy of the top of the barrier as a function of d (···).

bation theory as well as from previous nonperturbative calculations. The $1s$ energy level is not promoted toward the continuum, but displays a local maximum at an intermediate distance. This maximum occurs near the critical distance $d_c=3.6$ a.u., where the shifted level crosses the top of the barrier (denoted by the dotted line). As the $1s$ resonance becomes an over-barrier resonance, its position begins to bend down towards the bottom of the conduction band. This qualitative behavior of the resonance position was found to be stable against the variation of the parameters in the potential [e.g., α, λ, and $z_q(d)$]. We extended the calculations to small distances where the validity of the surface potential is questionable because of the lack of self-consistency (indicated by a dashed line), and were able to trace the resonance down to distances $d\simeq 1$ a.u.

For the purpose of comparison are also plotted the data available from other calculations [7,8], which show a rapid upward promotion of the level. The difference between the present results and the result of Borisov, Teillet-Billy, and Gauyacq *et al.* [8] can be directly traced to the imagelike behavior of the potential at small distances. In fact, the level position of Ref. [8] closely follows the classical image shift $\sim 1/(4(d-z_0))$ down to $d\simeq 3$ a.u. The promotion toward the continuum results from the narrowing of the potential well between the proton and the singular repulsive potential at z_0, thereby ''squeezing out'' bound states to the point where they can no longer exist. By contrast, as the barrier height is diminished in the present calculation (Fig. 6) the atomic orbital mixes freely with the jellium resulting in a downward trend in the resonance position. The reason for the difference between our result and the data of Ref. [7] is not equally obvious as the input potentials are more similar. One possible source of the discrepancy could be an inappropriate choice of the Sturmian parameter in the basis functions, which in Ref. [7] was chosen to represent the $n=2$ state correctly in combination with rather small basis sizes (49–64 states). Another source could be the difficulty of identifying the resonance trajectory in the complex E_r-E_i plane. It is easily possible to pick up spurious resonances. This happened, in fact, in an early stage of our calculation, and was recognized only after the resonant wave functions were analyzed. A very dense mesh in d is required in the over-barrier region in order to permit proper identification of the resonance.

The present result for the resonance position provides a smooth connection between the value in front of the surface and inside the bulk. Various calculations for the energy of the ground state of hydrogen in jellium with an electron density of aluminum predict a very weakly bound doubly occupied state as H^- or a low-lying near-threshold resonance [13,14,47]. Irrespective of the inherent uncertainties, these calculations agree in the position of a resonant or a bound state to lie near the bottom of the conduction band toward which our results converge. The smooth transition from the surface to bulk is not surprising, since the surface potential generated by the density fluctuation at the surface goes smoothly over into a screened bulk potential when the external charge recombines with the exchange and correlation hole.

While the quantitative accuracy of the energy in the immediate vicinity of the surface ($d\leqslant 2$ a.u.) should be viewed with caution, the correct qualitative behavior as $d\to 0$ translates into significant differences at intermediate distances which are *quantitatively* significant. For example, charge transfer into $H(1s)$ near an Al surface is expected to occur in the vicinity of the ''freezing distance'' of $d=4$ a.u. [44]. Here the energy shift relative to the vacuum level is about 33% smaller than previously calculated.

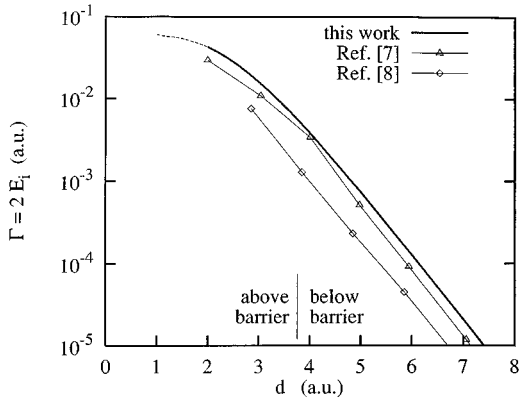

FIG. 9. Width of the $H(1s)$ resonance [$\Gamma=2\,\mathrm{Im}(E)$] as a function of d; —, present result; △, Ref. [7]; ◇, Ref. [8].

Another test for the present calculation is the physisorption energy

$$E_{\mathrm{ph}}=V_p(d)-(E_{1s}(\infty)-E_{1s}(d)) \tag{42}$$

on a metal surface. A calculation of the total energy of the hydrogen atom using the ground-state data obtained with a simple ionic image potential yields a physisorption energy close to zero, nearly independent of the distance. Our calculation yields a physisorption energy of $E_{\mathrm{ph}}=-1.4$ eV at $d=2$ a.u. in close agreement with the LDA results of Hjelmberg [13] ($E_{\mathrm{ph}}=-1.2$ eV) at this distance. This result could be further improved by taking into account the interaction between the ion core and the smeared-out electronic image charge determined from the electron density $|\phi_k^Q(\tilde{\mathbf{r}};E_k)|^2$ as given in Eq. (20). This would correspond to the first iteration in a self-consistent treatment.

B. Level width

Significant differences to previous calculations can also be observed in the width of the resonance, Γ, the imaginary part of the complex eigenvalue E, as shown in Fig. 9. For large distances, the width of the resonance decays approximately exponentially as expected for ''thick-barrier'' tunneling. Since the potential barrier in our present calculation is significantly lower than the one for the simple image potential used in Ref. [8], the large discrepancy by about a factor of 8 is easily understood in terms of a semiclassical Wentzel-Kramers-Brillouin (WKB) estimate. The WKB transmission coefficient W, and hence Γ, depend exponentially on the product of the width of the barrier and the square root of its height (difference between energy level and potential at the top of the barrier). Since the present potential is much closer to the one employed in Ref. [7], better agreement for $\Gamma/2$ in this regime is to be expected. The present values are nevertheless larger by about a factor of 2, which may be due to

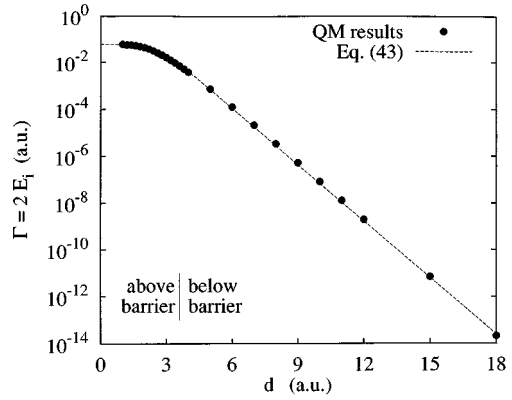

FIG. 10. Width of the H(1s) resonance: ●, as obtained with the CCS; ---, from Eq. (43).

differences in the potential or the smaller basis size. (For higher excited states the differences are smaller [46].)

At a critical distance $d_c \approx 3.6$ a.u., the resonance crosses the top of the barrier separating the atomic well from the jellium. The 1s state becomes a broad ''over-barrier'' resonance, and the width begins to saturate with decreasing d. The behavior of the level width including this saturation can be approximated by [26]

$$\Gamma(d) = \frac{\Gamma_0}{1+\exp(\chi(d-d_c'))}, \tag{43}$$

where d_c' should be close to d_c. Γ decays exponentially for large distances and saturates near Γ_0 for small distances. Using only the quantum-mechanical result for Γ_0 and fitted values of $d_c'=2.6$ and $\chi=1.85$, this equation reproduces the numerical data remarkably well over the whole range of $d=1 \ldots 18$, as shown in Fig. 10.

C. Resonant wave function

The classical dynamics near the top of the barrier is crucial for the structure of resonances and for the charge-transfer process [26,48]. Properties of the classical phase-space structure are reflected in the wave functions. The stabilization method [see Eq. (20)] provides an efficient tool to determine the resonant wave function.

Figure 11 shows the adiabatic evolution of the resonant 1s wave function for a range of distances from the surface. At large distances ($d \geqslant 8$ a.u.) for which the level shift is described well even by the classical image potential $1/4(d-z_0)$ the distortion of the contour lines is barely noticeable, i.e., the wave function is hardly perturbed by the presence of the surface [Fig. 11(a)].

At intermediate distances (around 7 a.u.), an increasing leakage current manifests itself in the outgoing wave front of the continuum portion of the resonant state which ''propagates'' towards the surface as d decreases [Fig. 11(b)]. In the region below $d=5$ a.u., where the level shift deviates from the simple image potential, this outgoing probability flux becomes sizeable [Fig. 11(c)]. The magnitude of the outgoing part of the wave function increases as the energy level approaches the top of the potential barrier, which it crosses at the critical distance d_c (here $d_c \simeq 3.6$ a.u.). The lowering of the barrier has opened a channel along which a considerable probability transfer to the solid can occur classically [Fig. 11(d)]. A morphological change of the resonant 1s wave function becomes clearly visible as a significant portion of the wave function now lies below the jellium edge with a peak in probability density split off the main lobe.

As d is further decreased, we observe a sequence of those secondary lobes moving inside the metal. However, the electron does not become delocalized at once because it is still dynamically confined by the potential well due to above-barrier reflection. It should be emphasized, however, that despite the strong distortion of the atomic state, the bound-state

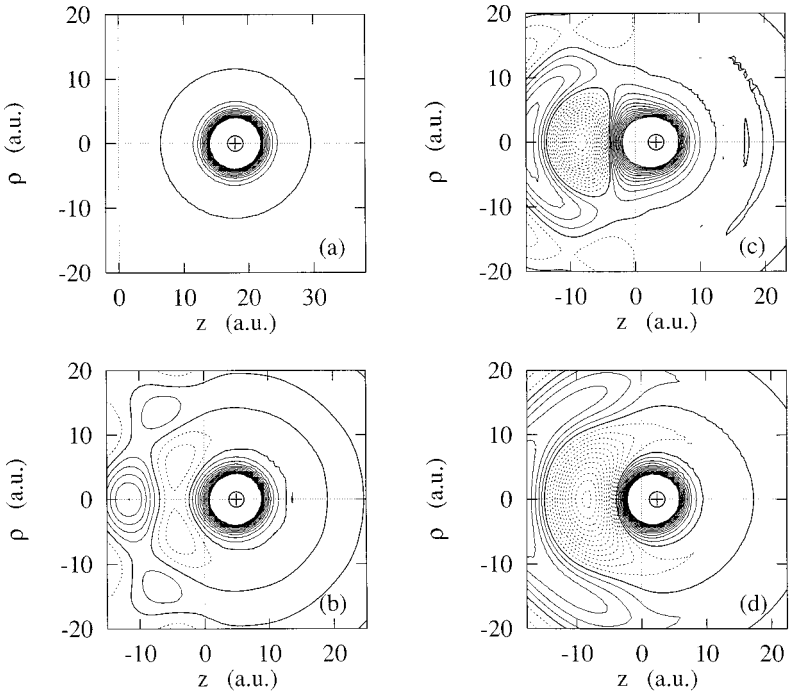

FIG. 11. Contour plot of resonant H(1s) wave function $\phi_{1s}^{Q}(\mathbf{r};E_{1s};d)$ in front of Al at $d=18$ a.u. (a), $d=5$ a.u. (b), $d=3.2$ a.u. (c), and $d=2.4$ a.u. (d). The surface is at $z=0$, the ion position is marked with a $\oplus$. Thick solid lines, $\phi_{1s}^{Q}=0$; thin solid lines, $\phi_{1s}^{Q}>0$; thin dashed lines, $\phi_{1s}^{Q}<0$. Contours from -3×10^{-2} to 3×10^{-2} in increments of 2×10^{-3}.

portion of the resonant wave function remains well localized around the ion core, and traceable down to very small distances. This observation is important in the context of the current controversial discussion as to the existence of atomic resonances in the vicinity of the surface. Our results demonstrate that they remain well defined in the region where over-barrier transitions become possible.

V. SEMICLASSICAL APPROXIMATION

It is of considerable conceptual and practical interest to inquire about the extent to which atomic resonances can be accounted for semiclassically. The conceptual interest lies primarily in its connection to classical models for charge transfer near the surface [26]. From a practical point of view, the semiclassical approximation provides a tool to treat high n states of multiply charged ions approaching the surface. First WKB calculations were performed by Janev and coworkers [49]. Questions have been raised [7] as to the validity of this approach. We focus in the following on the calculation of the level width Γ, or, equivalently, the transition rate for electron transfer from the atomic orbital to the band structure. It is equally possible to determine the level position using an Einstein-Brillouin-Keller multidimensional WKB quantization, exploiting the fact that the problem remains approximately separable. From here on all coordinates refer again to the ionic core as the origin and we drop the tilde. Since the following is mainly based on Refs. [49–53], we will focus on the interesting aspects of our calculation.

The system is rotationally symmetric about the surface normal, and the leakage current passes primarily through a small cylindrical region around this axis. Parabolic coordinates [50,52]

$$\zeta = r + z, \quad \eta = r - z, \quad \varphi = \arctan \frac{y}{x} \tag{44}$$

are therefore appropriate. The region near the barrier for which the solution of the Schrödinger equation is sought corresponds to $\zeta \ll \eta$. Hence we consider the reaction coordinate $\eta \simeq -2z$, which allows to simplify the Hamiltonian and to write the potential as

$$V^{\mathrm{tot}}(\eta) = -\frac{2Z}{\eta} + V^{\mathrm{surf}}(\eta). \tag{45}$$

The transition rate W, i.e., the probability flux with a velocity, v_z through an area S perpendicular to the z axis, is given by [50]

$$W = \int_S |\Phi(\zeta, \eta, \varphi)|^2 v_z \, dS. \tag{46}$$

Here $dS = 1/2\,\eta d\zeta d\varphi$, and $\Phi(\zeta,\eta,\varphi)$ is the WKB wave function [50,51] of the system. Assuming $\eta \gg \zeta$, the velocity component across the barrier, v_z, is related to the quasimomentum $p_\eta(\eta)$ as $v_z = p_\eta(\eta)/2$ with

$$p_\eta^2(\eta) = \left[-\frac{\gamma^2}{4} + \frac{\beta}{\eta} - \tfrac{1}{2} V^{\mathrm{surf}}(\eta/2) + \frac{1-m^2}{4\eta^2} \right], \tag{47}$$

where $\gamma = \sqrt{-2E_r}$ and $\beta = Z - \gamma(m+1)/2$, and the magnetic quantum number $m = 0$ for the $1s$ state. Figure 12 shows a plot of the square of the quasimomentum, $p_\eta^2(\eta)$, from Eq. (47) for $d = 10$. Positive values of the ''local'' kinetic energy of the electron correspond to the motion of the electron in the classically allowed region, whereas negative values correspond to classically forbidden tunneling motion.

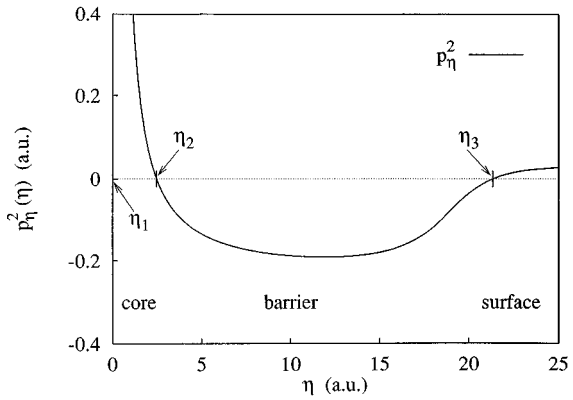

FIG. 12. Plot of $p_\eta^2(\eta)$ from Eq. (47) for $d = 10$. $\eta_{i=1\ldots3}$ denotes the classical turning points of the system, where $p_\eta^2(\eta_t) = 0$. $\eta_0 = 0$ corresponds to the position of the ion core.

For energy values below the top of the potential barrier, we assume a leakage current small enough so that the wave function can be normalized in the potential well (thick barrier approximation). Equation (46) in this limit becomes

$$W \simeq W_\eta = \frac{\exp(-2\int_{\eta_2}^{\eta_3} |p_n(\eta)|\, d\eta)}{\int_{\zeta_1}^{\zeta_2} d\zeta \int_{\eta_1}^{\eta_2} d\eta \left(1 + \dfrac{\zeta}{\eta}\right) \dfrac{\exp(-\zeta)}{p_\eta(\eta)}}, \tag{48}$$

where $\eta_{i=1\ldots3}$ and $\zeta_{j=1\ldots2}$ denote the classical turning points in the respective parabolic coordinates $[p_\eta^2(\eta_i) = p_\zeta^2(\zeta_j) = 0]$, counted from the origin on (Fig. 12). The numerator in Eq. (48) is the barrier penetration factor T along the reaction coordinate η, while the denominator is the normalization integral related to the classical orbital period, averaged over ζ.

For the region near the barrier top we employ the uniform WKB (UWKB) for the transition rate [53], which allows us to study the above-barrier region. We exploit the fact that the potential barrier along the reaction coordinate can be locally approximated by an inverted parabola

$$V(\eta) = V_{\mathrm{top}} - \tfrac{1}{2}\omega^{*2}(\eta - \eta_{\mathrm{top}})^2, \tag{49}$$

where ω^* is obtained from the second derivative of the full potential,

$$\omega^*(\eta_{\mathrm{top}}) = \left[-\frac{d^2 V(\eta, d)}{d\eta^2} \right]_{\eta = \eta_{\mathrm{top}}}^{1/2}. \tag{50}$$

The barrier penetration factor given by the numerator in Eq. (48) is now replaced by [53]

$$T = [1 + \exp(-2\pi\epsilon)]^{-1}, \tag{51}$$

where

$$\epsilon = \begin{cases} -\dfrac{1}{\pi} \displaystyle\int_{\eta_2}^{\eta_3} |p_\eta(\eta)|\, d\eta & \text{if} \quad E_r(d) < V_{\mathrm{top}} \\ +\dfrac{i}{\pi} \displaystyle\int_{\eta_-}^{\eta_+} p(\eta)\, d\eta & \text{otherwise.} \end{cases} \tag{52}$$

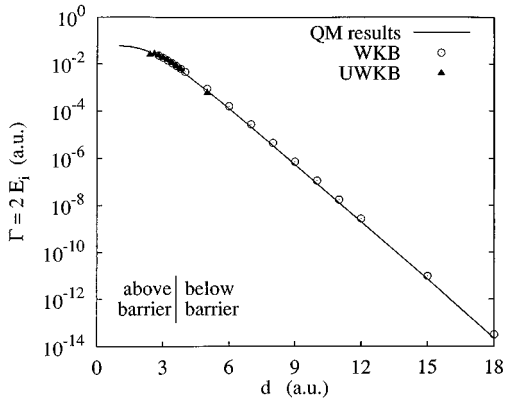

FIG. 13. Width of the H($1s$) resonance [$\Gamma=2\,\mathrm{Im}(E)$] as a function of d: Comparison between quantum-mechanical (—) and semiclassical results (◎, WKB; ▲, UWKB) calculations (see text).

Here $\eta_{2,3}$ are again the classical turning points, i.e., zeros of $p_\eta^2(\eta)$ on the real axis, while $\eta_\pm$ are the zeros of $p_\eta^2(\eta)$ in the complex plane, i.e., $p_\eta^2(\eta_\pm)=0$, and $\eta_{\mathrm{top}}=(\eta_+ + \eta_-)/2$. For the quadratic approximation for the barrier [Eq. (48)], Eq. (52) can be reduced to

$$\epsilon=(E_r - V_{\mathrm{top}})/\omega^*. \tag{53}$$

For η values near the jellium edge ($\eta=2d$), the approximation of the potential in terms of an inverted parabola [Eq. (49)] fails completely, since the flat background potential of the jellium dominates in this region.

We now evaluate W using the energy values $E_r(d)$ obtained from the quantum-mechanical calculations. The resulting widths (Fig. 13) agree with the quantum-mechanical widths to within 15% in both the below-barrier region $d \geqslant d_c$ as well as in the over-barrier region (down to $d \simeq 2.4$). The uncertainty introduced by the semiclassical approximation is much smaller than the differences between quantum calculations employing different approximations to the surface potential. It should be noted that the present calculation is effectively one dimensional in the reaction coordinate η, while the ζ degree of freedom is averaged over in the normalization factor. A fully three-dimensional WKB calculation should yield even better agreement, since it takes into account the lateral variation of the potential surface.

VI. CONCLUSIONS

In summary, we have presented results on the adiabatic evolution of the H($1s$) resonance near a jellium surface with the electronic density of aluminum, using complex rotation and stabilization techniques. Both methods were found to yield results of the resonance parameters of comparable accuracy. While the complex rotation method is more efficient in accurately determining simultaneously the position and the width, the stabilization technique provides a more efficient tool to determine the position alone, and has the added benefit that resonant wave functions can be readily extracted.

The level position follows the classical image shift formula only for distances $d \gg d_c$, where d_c is the distance at which the $1s$ resonance becomes an overbarrier resonance. It reaches a maximum near d_c, then bends down toward the bottom edge of the conduction band as $d < d_c$, and appears to connect smoothly with results for resonances around a proton in the bulk jellium. The level width decreases exponentially with the distance for $d \geqslant d_c$ while saturating for smaller distances. This behavior could be reproduced in semiclassical calculations for both the below- and above-barrier regions. Semiclassical mechanics was shown to provide accurate estimates for the resonances width and conceptual insights into the electronic dynamics near the surface. The resonant wave functions undergo, near d_c, a morphological change with an increasing delocalization and shift of probability density toward the metal.

Level width and position data reported in the present paper differ significantly from previously available data [7,8], in particular in the vicinity of the surface. The discrepancies can be traced primarily to the different choices for the surface potentials. Discrepancies for the level shift reported in [8] can be attributed to the use of a divergent ionic image potential. Overall, the present resonance data are closer to the results of Ref. [7] than to Ref. [8].

Extensions are currently under investigation along three directions: (a) the adiabatic evolution of highly excited resonances ($n \gg 1$), (b) the study of the region for $d \ll d_c$ using nonlinear density-functional theory [33], and (c) the treatment of nonadiabatic transitions in ion-surface scattering.

We note that after completion of this work we learned that Flores *et al.* [54] obtained a behavior of the $1s$ level position similar to ours by means of a density-functional calculation near the surface. This observation is in qualitative agreement with the present results.

ACKNOWLEDGMENTS

Helpful discussions with J. P. Gauyacq, A. G. Borisov, P. Nordlander, and C. Reinhold are gratefully acknowledged. Work was supported by the U.S. Department of Energy, Office of Basic Energy Sciences, Division of Chemical Sciences, under Contract No. DE-AC05-96-OR22464 with Lockheed Martin Energy Research, Inc.

[1] *Proceedings of the VII International Conference on the Physics of Highly Charged Ions (HCI-94)*, edited by F. Aumayr, G. Betz, and H. P. Winter [Nucl. Instrum. Methods Phys. Res. Sect. B **98**, 1 (1995)].

[2] B. H. Bransden and M. R. C. McDowell, *Charge Exchange and the Theory of Ion-Atom Collisions* (Clarendon, Oxford, 1992).

[3] J. W. Gadzuk, Surf. Sci. **6**, 133 (1967); **6**, 159 (1967).

[4] M. Remy, J. Chem. Phys. **53**, 2487 (1970).

[5] J. Burgdörfer, E. Kupfer, and H. Gabriel, Phys. Rev. A **35**, 4963 (1987).

[6] U. Thumm and P. Kürpick, Bull. Am. Phys. Soc. **41**, 1060 (1996).

[7] P. Nordlander and J. C. Tully, Phys. Rev. Lett. **61**, 990 (1988); Surf. Sci. **211/212**, 207 (1989); Phys. Rev. B **42**, 5564 (1990).

[8] D. Teillet-Billy and J. P. Gauyacq, Surf. Sci. **239**, 343 (1990);

A. G. Borisov, D. Teillet-Billy, and J. P. Gauyacq, Nucl. Instrum. Methods Phys. Res. Sect. B **78**, 49 (1993).
[9] P. Hohenberg and W. Kohn, Phys. Rev. **136**, 864 (1964).
[10] W. Kohn and L. J. Sham, Phys. Rev. **140**, A1133 (1965); L. J. Sham and W. Kohn, *ibid*. **145**, 561 (1966).
[11] N. D. Lang and W. Kohn, Phys. Rev. B **1**, 4555 (1970); **3**, 1215 (1971); **7**, 3541 (1973).
[12] O. Gunnarsson and H. Hjelmberg, Phys. Scr. **11**, 97 (1975).
[13] H. Hjelmberg, Phys. Scr. **18**, 481 (1978).
[14] C. O. Almbladh, U. von Barth, Z. D. Popovic, and M. J. Scott, Phys. Rev. B **14**, 2250 (1976).
[15] V. A. Mandelshtam, T. R. Ravuri, and H. S. Taylor, Phys. Rev. Lett. **70**, 1932 (1993).
[16] J. Müller, X. Yang, and J. Burgdörfer, Phys. Rev. A **49**, 2470 (1994).
[17] J. Aguilar and J. M. Combes, Commun. Math. Phys. **22**, 269 (1971), E. Baslev and J. M. Combes, *ibid*. **22**, 280 (1971).
[18] W. Reinhardt, Ann. Phys. Rev. Chem. **33**, 232 (1982).
[19] B. R. Junker, in *Advances in Atomic and Molecular Physics*, edited by Sir David Bates and Benjamin Bederson (Academic, New York, 1982).
[20] Y. K. Ho, Phys. Rep. **99**, 1 (1983).
[21] S. A. Deutscher, X. Yang, and J. Burgdörfer, Nucl. Instrum. Methods Phys. Res. Sect. B **100**, 336 (1995); S. A. Deutscher, X. Yang, J. Burgdörfer, and H. Gabriel, *ibid*. **115**, 152 (1996).
[22] J. N. Bardsley, Case Stud. At. Phys. **4**, 299 (1974).
[23] R. H. Garvey, C. H. Jackman, and A. E. S. Green, Phys. Rev. A **12**, 1144 (1975), and references therein.
[24] H. Winter, Europhys. Lett. **18**, 207 (1992).
[25] J. Burgdörfer and F. W. Meyer, Phys. Rev. A **47**, R20 (1993).
[26] J. Burgdörfer, in *Review of Fundamental Processes and Applications of Atoms and Ions*, edited by C. D. Lin (World Scientific, Singapore, 1993).
[27] M. Rotenberg, Adv. At. Mol. Phys. **6**, 233 (1970).
[28] H. Feshbach, Ann. Phys. (N.Y.) **19**, 287 (1962).
[29] O. Gunnarsson and R. Jones, Phys. Scr. **21**, 394 (1980).
[30] P. J. Jennings, R. O. Jones, and M. Weinert, Phys. Rev. B **37**, 6113 (1988); P. J. Jennings and R. O. Jones, Adv. Phys. **37**, 341 (1988).
[31] S. Ossicini, C. M. Bertoni, and P. Gies, Europhys. Lett. **1**, 661 (1986).
[32] P. A. Serena, J. M. Soler, and N. García, Phys. Rev. B **34**, 6767 (1986); **37**, 8701 (1988).
[33] A. G. Eguiluz, Phys. Rev. B **31**, 3303 (1985).
[34] A. G. Eguiluz and W. Hanke, Phys. Rev. B **39**, 10 433 (1989).
[35] D. Pines, *Elementary Excitations in Solids: Lectures on Phonons, Electrons, and Plasmons* (Benjamin, New York, 1963).
[36] M. Gell-Mann and K. A. Brueckner, Phys. Rev. **106**, 364 (1957).
[37] C. Kittel, *Einführung in die Festkörperphysik* (R. Oldenburg, München, 1989).
[38] F. J. G. de Abajo and P. M. Echenique, Phys. Rev. B **46**, 2663 (1992); F. J. G. de Abajo, Ph.D. thesis, The University of the Basque Country, San Sebastián, 1993; F. J. G. de Abajo and P. M. Echenique, Phys. Rev. B **48** 1399 (1993).
[39] R. H. Ritchie and A. L. Marusak, Surf. Sci. **4**, 234 (1966).
[40] P. M. Echenique, R. H. Ritchie, N. Barberan, and J. Inkson, Phys. Rev. B **23**, 6486 (1981).
[41] H. Raether, in *Excitation of Plasmons and Interband Transitions by Electrons*, Springer Tracts in Modern Physics Vol. 88 (Springer-Verlag, Berlin, 1980).
[42] N. R. Arista, Phys. Rev. A **49**, 1885 (1994).
[43] K. J. Krane and H. Raether, Phys. Rev. Lett. **37**, 1355 (1976).
[44] H. Winter (unpublished).
[45] J. F. Annett and P. M. Echenique, Phys. Rev. B **34**, 6853 (1986).
[46] S. A. Deutscher, X. Yang, and J. Burgdörfer (unpublished).
[47] J. Friedel, Philos. Mag. **43**, 153 (1952).
[48] J. Burgdörfer, P. Lerner, and F. W. Meyer, Phys. Rev. A **44**, 5674 (1991).
[49] R. K. Janev, J. Phys. B **7**, 1506 (1974); T. P. Grozdanov and R. K. Janev, Phys. Lett. A **65**, 396 (1978).
[50] H. A. Bethe and E. E. Salpeter, *Quantum Mechanics of One- and Two-Electron Atoms* (Plenum, New York, 1977).
[51] L. D. Landau and E. M. Lifschitz, *Quantenmechanik* (Akademie-Verlag, Berlin, 1979).
[52] P. P. Morse and H. Feshbach, *Methods of Theoretical Physics*, International Series in Pure and Applied Physics (McGraw-Hill, New York, 1953).
[53] M. S. Child, *Semiclassical Mechanics with Molecular Applications*, International Series of Monographs on Chemistry (Clarendon Press, Oxford, 1991).
[54] F. Flores, J. Meriro, F. J. Garcia-Vidal, N. Lorente, and R. Monreal (private communication).